ACS APPLIED
ENERGY MATERIALS

Article

Photocatalytic Activity and Electron Storage Capability of TiO$_2$ Aerogels with an Adjustable Surface Area

Alexandra Rose, Anja Hofmann, Pascal Voepel, Barbara Milow, and Roland Marschall*

Cite This: https://doi.org/10.1021/acsaem.2c02517

Read Online

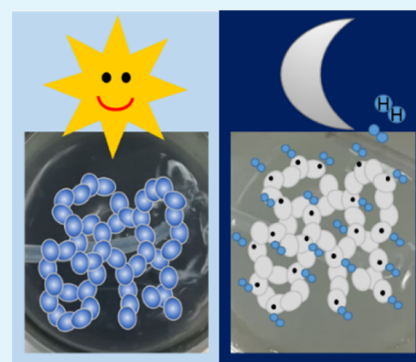ACCESS | 📊 Metrics & More | 📖 Article Recommendations | 🗎 Supporting Information

ABSTRACT: Mesoporous TiO$_2$ aerogels with a surface area larger than 600 m^2 g^{-1} have been prepared *via* acid-catalyzed sol−gel synthesis and supercritical drying. Varying temperature treatments in air result in changes in the morphology of the aerogels and their specific surface area. Interestingly, the ability to store photogenerated electrons in the surface states of the aerogels upon illumination of dispersions in water−methanol mixtures increases at lower calcination temperatures. Additionally, the extent of electron storage capability also depends on hole scavenger concentration. Increasing the calcination temperature to 500 °C results in a decreased surface area and electron storage capability but increased hydrogen evolution rates. Finally, nitrogen reduction to ammonia in the dark is performed with photogenerated stored electrons in TiO$_2$ aerogels, separating the charge carrier photogeneration from the dark reduction reaction.

1. INTRODUCTION

Aerogels are unique 3D mesoporous materials composed of interconnected porous networks which exhibit high surface areas, open pores, and low densities.[1,2] The sol−gel process is a prominent technique to synthesize such aerogels since it is a simple method and requires no complex setup. Several synthesis parameters can be varied to control the nanoscale structure and physicochemical properties.[3,4] It has been demonstrated that high surface areas could be obtained in amorphous titania aerogels based on chloride and alkoxide precursors, followed by hydrolysis and condensation reactions to form a wet gel,[5,6] which is further dried, for example, supercritically, to prevent the porous structure from collapsing.[1] Reported surface areas for amorphous TiO$_2$ aerogels are in the range of 466 to 733 m^2 g^{-1}.[4,6−8] The ability to control the sol−gel process for synthesizing aerogels is a powerful tool for designing a suitable and efficient catalyst. A high specific surface area and open porosity of aerogels favor the adsorption and diffusion of reactants, thereby offering many active reaction sites and their accessibility for photocatalytic reactions.[9] The interconnected network of nanoparticles offers additionally long diffusion pathways for photogenerated electrons.

Aerogels were reported as suitable catalysts for photocatalytic applications, for example, the degradation of dyes or organic substances and hydrogen evolution.[10−14] Especially, TiO$_2$ and composite aerogels are promising materials for efficient photocatalysis, due to the high number of reactive sites and improved charge separation.[15,16] Both the polymorphic forms of TiO$_2$ and the morphological and structural characteristics were reported as crucial factors for photocatalysis. Different synthesis procedures for TiO$_2$ aerogels are reported in the literature to optimize the synthesis parameters and consequently the morphological and structural characteristics with regard to photocatalytic hydrogen evolution.

Parayil *et al.* investigated the synthesis parameters using alkoxide precursors for TiO$_2$ aerogel synthesis *via* high-temperature supercritical drying.[17] Luna *et al.* reported TiO$_2$ aerogels assembled from crystalline preformed nanoparticles which showed efficient hydrogen generation.[10] Recently, Niederberger *et al.* presented similar titania-based aerogels and their ability for hydrogen production based on water/methanol vapors. They reported gas-phase hydrogen evolution rates of up to 340 μmol g^{-1} h^{-1} for a 0.5 wt % Pd decorated TiO$_2$ aerogel under irradiation with a 375 nm LED.[18] TiO$_2$−Pt composites were reported by Lin *et al.* and Puskelova *et al.*[19,20] They described the dependency of the hydrogen evolution rate on the Pt particle size and loading on TiO$_2$, reflecting the number of reactive sites. Lin *et al.* reported a hydrogen evolution rate of 18.3 μmol g^{-1} h^{-1} at 30 °C for a titania aerogel with 84.5 m^2 g^{-1} surface area after calcination for 10 h at 500 °C. After decoration with 0.5 wt % Pt, an evolution rate

ACS Publications

A

of 328 μmol g^{-1} h^{-1} was obtained. These values correspond to ~1 and 16.4 μmol h^{-1}, and the evolution rates were higher compared to those of P25 nanoparticles and hydrothermally prepared TiO$_2$ nanocrystals.[19] Puskelova et al. obtained the highest hydrogen evolution rate of 7.2 mmol h^{-1} g^{-1} (720 μmol h^{-1}) for Pt-decorated anatase aerogels calcined at 500 °C for 30 min with 1 wt % Pt and a Pt particle size of 5.75 nm.[21] With intensity-modulated photovoltage spectroscopy and photocurrent spectroscopy measurements on TiO$_2$ aerogels synthesized with different weight fractions of sol–gel precursors, DeSario et al. were able to show that trapping sites are the reactive sites in photocatalytic hydrogen generation.[15] This could be concluded due to differences in the lifetime and mobility of photogenerated electrons. Hydrogen generation increased with increased sol–gel precursor concentration. By use of UV–vis and EPR spectroscopy, Di Iorio et al. found an improved electron storage capacity for TiO$_2$ ethanolic sols with an increase of the titanium to water molar ratio.[22] Panayotov et al. reported that photogenerated electron–hole pairs in TiO$_2$ aerogels are more efficiently separated compared to commercial TiO$_2$ nanoparticles and that the density of excited-state electrons is higher in these aerogels.[23]

Besides the aerogel structure, the crystal structure also has an influence on the charge carrier lifetime. Sachs et al. performed transient absorption spectroscopy measurements on the most commonly used TiO$_2$ crystal phases, that is, rutile and anatase. They found a faster recombination rate for the rutile crystal phase, and for both polymorphs the surface recombination is the most important factor for the charge carrier lifetime.[24]

There are several examples in the literature which report the storage of photoexcited electrons in semiconductor materials and the use of these stored electrons for reduction reactions in the dark. Bahnemann et al. reported the trapping of electrons close to the surface of colloidal TiO$_2$ with the formation of Ti^{3+} states in the presence of a hole scavenger, which was characterized by broad absorption with a maximum at 650 nm.[25] By employing the stopped-flow technique and UV–vis spectroscopy, they investigated the reduction reaction of such stored electrons with silver ions,[26] gold ions,[27] and other electron acceptors in detail.[28,29] In 2011, they showed, for the first time, that photoexcited electrons stored in TiO$_2$ can reduce dinitrogen.[30] Since then, reports about the electron storage of different materials,[31] including WO$_3$,[32,33] copper complexes,[34] and carbon nitrides,[35] were published. In the case of cyanamide-functionalized polymeric networks of heptazine units, 4-methylbenzyl alcohol is necessary as a hole acceptor to store electrons in the material. In contrast, an aqueous methanol solution with a concentration of 0.02 mol L^{-1} is already enough to extract photoexcited holes from TiO$_2$ and to store photoexcited electrons.[30] The addition of a cocatalyst, such as Pt or other metal cocatalysts, to a photocatalyst storing photoexcited electrons in an aqueous solution leads to the formation of hydrogen.[26,27,35,36]

There are also some reports on the storage of photoexcited electrons in photoelectrodes. Amal et al. showed for WO$_3$ photoelectrodes that higher calcination temperatures lead to improved crystallinity but reduced electron storage. The photoelectrochemical H$_2$ evolution activity also increased as long as the contact between WO$_3$ and the substrate was sufficient.[37] They presented in another work that WO$_3$ films can be charged using an electrolyte with alkali cations and that

these charges can be used in dark conditions.[32] These films could also be recharged. Kamat and Takai showed that photocatalytically deposited Ag on TiO$_2$ leads to an improved photoelectrochemical performance with about 2 times higher photocurrent in TiO$_2$/Ag films compared to that in unmodified TiO$_2$ films.[38] The authors explained this improved activity by capturing photogenerated electrons and the more negative Fermi level. They also found a dependency of electron storage on the amount of deposited Ag, with an optimum capacity at 8.6 μM for a suspension with 5.8 mM TiO$_2$. They quantified the stored electrons by titration with methylene blue and found that the electron storage is best for Ag-modified TiO$_2$ compared to pristine, Au-modified, or Pt-modified TiO$_2$.[42]

In the present work, we report a detailed investigation on the photocatalytic and electron storage properties of mesoporous TiO$_2$ aerogels prepared via a novel approach for a modified acid-catalyzed sol–gel synthesis with subsequent supercritical drying and different heat treatments in air. All prepared TiO$_2$ aerogels exhibit the anatase crystal structure to exclude the influence of composite formation on the photocatalytic activity and electron storage ability of the aerogels. The influence of physical properties, especially the surface area and crystallinity, on the ability to store electrons in water–methanol slurry and on hydrogen evolution is discussed. Quantification experiments of the stored electrons via reduction reactions in the dark will be presented. Furthermore, methanol concentration-dependent measurements on samples with high electron storage ability are presented. We show the possibility of electron storage optimization by adjustment of crystallinity, surface area, and concentration of a sacrificial agent, for which TiO$_2$ aerogel materials offer the possibility of tailoring the surface area and crystallinity over a wide range. Through an experiment for nitrogen reduction in the dark yielding ammonia, we pave the way for a possible ammonia-on-demand application of the herein-synthesized photocharged aerogels besides hydrogen generation.

2. EXPERIMENTAL SECTION

2.1. Chemicals. Titanium(IV) tetraisopropoxide (98%, Merck), hydrochloric acid (37%, ACS reagent, Sigma-Aldrich), ethanol (CHEMSOLUTE, denatured with MEK, IPA, and Bitrex, 99.8%), methanol (99.9%, Fisher Chemical), hexachloroplatinate(IV) hydrate (99.995%, Carl Roth), and Hombikat UV 100 (99%, Sachtleben Chemie) were used as received.

2.2. TiO$_2$ Aerogel Synthesis (Scheme 1). TiO$_2$ gels were prepared with an acid (HCl)-catalyzed sol–gel method using titanium(IV) isopropoxide (TTIP) as the precursor. The molar ratio of TTIP/ethanol/acid/water was kept constant of 1:26:0.1:4. A solution containing TTIP in ethanol (EtOH) was prepared under magnetic stirring at 0 °C. Hydrochloric acid was added after few minutes. Deionized water was added dropwise to the solution. A gel was formed after few minutes. Gels were aged for 7 days at 50 °C, washed in isopropanol four times, and dried with CO$_2$ at supercritical conditions (60 °C, 115 bar, flow rate 15–20 kg/h). As-formed aerogels, excluding the as-synthesized aerogel, were thermally treated in air at 300, 400, and 500 °C for 10 h (heating rate: 10 K min^{-1}).

2.3. Characterization. XRD measurements were performed on a Bruker D8 ADVANCE X-ray diffractometer using a Cu Kα radiation source and a LYNXEYE XE-T detector. The diffraction data were collected in the range of 15–90° 2θ with a step size of 0.01°. The crystallite sizes were estimated using Bruker EVA software by calculating the integral breadth from the XRD pattern. Phase quantification and determination of amorphous/crystalline phase

Scheme 1. Schematic Presentation of the Synthesis Procedure and Images of TiO$_2$ Wet Gel (Left) and Aerogel (Right)
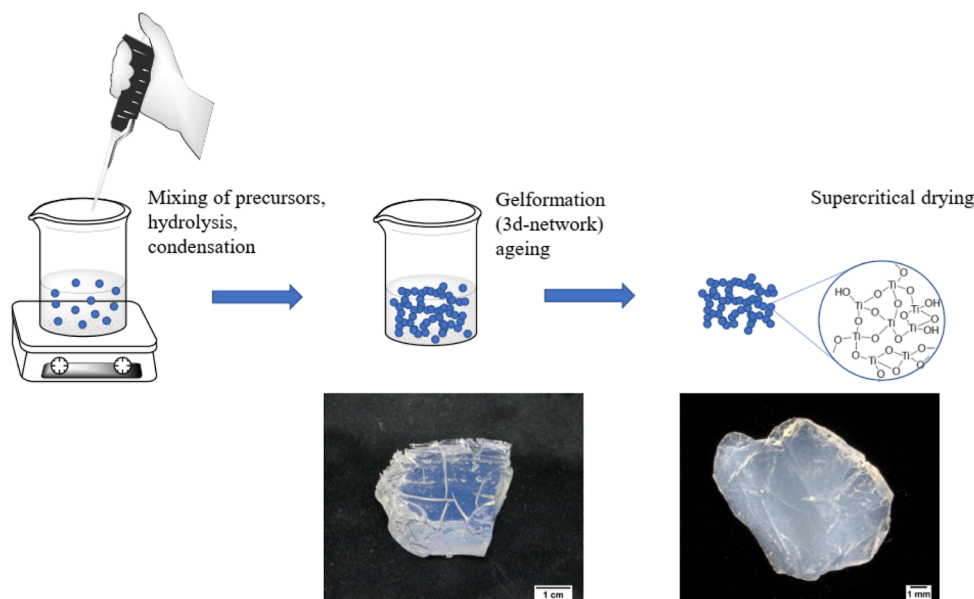
was performed by the Rietveld method implemented in Topas using CeO$_2$ as the internal standard.

Raman spectra were recorded using an XploRA PLUS Raman spectrometer (HORIBA Scientific) with an operating wavelength of 532 nm.

The specific surface area was determined *via* N$_2$ physisorption measurements at 77 K on a Micromeritics 3Flex instrument in a partial pressure range of $0.05 < p/p^0 < 0.3$ using the Brunauer–Emmett–Teller (BET) method. The total pore volume of the samples was obtained from the N$_2$ desorption isotherms at a partial pressure of 0.98, and the pore size distribution was obtained using the Barrett–Joyner–Halenda (BJH) model. Prior to physisorption analysis, the samples were outgassed at 60 °C for 12 h on a Micromeritics VacPrep Gas Adsorption Sample Preparation Device.

SEM images were taken with a Zeiss Ultra 55 electron microscope using an accelerating voltage of 3 kV. The samples were coated with platinum using a Baltec sputter coater prior to measuring.

TEM analysis was performed with a Philips Tecnai F30 operated at 300 kV. D-spacing was determined from TEM images using ImageJ.

A PerkinElmer Lambda 750 UV/vis/NIR spectrometer, equipped with a Praying-Mantis mirror unit from Harrick, was used to record the diffuse reflectance of the powdered aerogels with a step size of 1 nm. The used white standard was a Spectralon pellet. The spectra were converted into absorption spectra using the Kubelka–Munk function. Tauc plots were used to estimate the band gaps. For the estimation of the absorbance of the dispersions, the spectrometer was equipped with an integrating sphere, and the dispersion was stirred during the measurements of the diffuse reflectance. The spectra were converted to absorbance spectra. Three measurements were performed for every data point, and error was determined.

The lamp spectrum was measured with a Flame spectrometer from Ocean Insight.

2.4. Photocatalytic Test Experiments. For all photocatalytic experiments, ultrapure water with TOC = 2 ppb was used. The experiments were conducted with a 300 W Xe lamp (Quantum Design, lamp spectrum is shown in Figure S1) in a top-irradiated glass reaction vessel. Measurements were all performed at 20 °C [ECO RE 1050G (Lauda) thermostat] under stirring. The system was flushed with argon 5.0 before the measurements to remove residual air. Detection of the evolved hydrogen was performed every 11 min using a GC2014 gas chromatograph from Shimadzu, equipped with a shin carbon ST column (Restek) and a thermal conductivity detector, using argon 5.0 as the carrier gas. The argon 5.0 flow rate for the measurements was set to 25 mL min^{-1} with a Bronkhorst mass flow controller.

The hydrogen evolution experiments with Pt photodeposition were carried out with a 100 mg aerogel sample dispersed in a mixture of 135 mL water and 15 mL methanol. The dispersion was irradiated for 100 min without cocatalyst. The lamp was turned off to wait until no hydrogen evolution was detected anymore; then, an aqueous solution of hexachloroplatinate(IV) hydrate was added *via* rubber sealing without opening the reactor to reach a loading of 0.0076 μmol m^{-2}. The lamp was turned on again after the hydrogen evolution peak was observed, and the sample was irradiated for another 100 min. Afterward, the lamp was turned off, and it was left to rest until the hydrogen evolution was zero. A certain amount of hexachloroplatinate(IV) hydrate was added to the calcined aerogel dispersion to reach the same loading amount of 0.1 wt % Pt as for the as-synthesized aerogel sample. The dispersions of the calcined aerogel samples were irradiated again for 100 min, the lamp was turned off, and the measurements were stopped after no hydrogen evolution was detected. Photographs of all dispersions were taken before the measurement and after each irradiation step. The samples with Pt deposited were washed with isopropanol three times and centrifuged at 1500 rpm. Then they were dried with CO$_2$ at supercritical conditions. XRD measurements were performed as described above to determine any changes in the sample.

For the experiments to detect the absorbance of the dispersions, 100 mg of the aerogel sample were dispersed in a mixture of 135 mL water and 15 mL methanol. After flushing with argon 5.0, a sample of approximately 2.5 mL dispersion was taken and filled in an argon-flushed closed cuvette, and the diffuse reflectance was measured in a PerkinElmer Lambda 750 UV/vis/NIR spectrometer, equipped with an integrating sphere under stirring. The aerogel dispersions were, afterward, irradiated for 100 min. 2.5 mL of the blueish dispersion was filled in an argon flushed cuvette, and the diffuse reflectance was measured immediately, 30, and 110 min after the sample was taken.

For the experiments of the dependency of the electron storage ability on the methanol concentration, 100 mg of the as-synthesized aerogel sample were dispersed in 150 mL aqueous methanol solutions with different methanol concentrations ranging from 0.02 to 19.7 mol L^{-1}. The dispersions were irradiated for 100 min. Photographs of the dispersions were taken directly after the irradiation.

For the nitrogen reduction reaction, 100 mg of the as-synthesized aerogel was dispersed in 150 mL of 2.5 mol L^{-1} aqueous methanol solution. The dispersion was irradiated for 100 min under the same conditions as for the absorbance detection measurements; the argon

5.0 flow rate was set to 50 mL min^{-1}. After the irradiation under argon 5.0, the carrier gas was switched to N_2. The flow rate was set to 50 mL min^{-1} N_2 for 7 h for the nitrogen reduction reaction in the dark. Afterward, a salicylate test was performed to determine the yield of NH_3 quantitatively.[39]

2.5. Electron Quantification Experiments. Electron quantification *via* Pt^{4+} reduction and hydrogen evolution was performed in the same reactor as described above. The reaction parameters were kept identical to the hydrogen evolution experiments. The argon 5.0 flow rate was set to 100 mL min^{-1}, and the hydrogen gas evolution was detected online using a mass spectrometer (Hiden HPR-20 Q/C) every 13 s. The samples were irradiated for 100 min, and it was left to rest until no hydrogen evolution from that irradiation was detected anymore (this time was set to zero). Then, 0.1 wt % Pt as precursor was added to the dispersion *via* a rubber sealing without opening the reactor, and it was left to rest until no hydrogen evolution in the dark was detected anymore.

3. RESULTS AND DISCUSSION

3.1. Sample Characterization. A synthesized TiO$_2$ wet gel (Scheme 1 left photograph) shows a transparent appearance. After supercritical drying, the as-synthesized TiO$_2$ aerogel (Scheme 1 right photograph) turns into a very light, brittle, and translucent aerogel. The translucency in the visible range indicates a small particle size and homogeneous pore distribution.[40]

The X-ray diffraction (XRD) patterns of the as-synthesized and calcined TiO$_2$ aerogels are shown in Figure 1. It can be
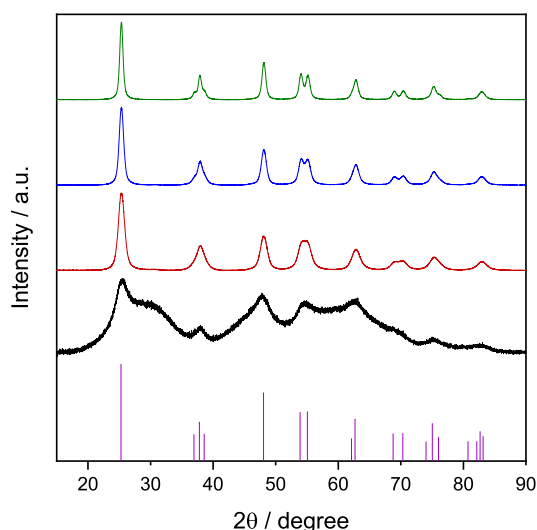

Figure 1. XRD patterns of the as-synthesized TiO$_2$ aerogel (black) and aerogels calcined at 300 °C (red), 400 °C (blue), and 500 °C (green). The reference line pattern of anatase TiO$_2$ (PDF-21-1272) is shown for comparison. Normalized data is in the range of 0 to 100, related to the highest signal.

observed that, surprisingly, the as-synthesized TiO$_2$ aerogel (please see the Experimental Section for details) is semi-crystalline. The broad diffraction peaks represent a high amorphous content, but the main reflections at 25.28 and 48.05° 2θ agree with the main reflections of anatase TiO$_2$ (PDF-21-1272). TiO$_2$ nanostructures which are synthesized using TTIP were reported to be crystalline (anatase) when ambiently dried or dried at, for example, 60 °C.[41,42] However, in our case, the TiO$_2$ gels were supercritically dried, which is generally reported in the literature leading to amorphous aerogels. Varying the synthesis conditions, for example, type or

amount of catalyst, without any addition/assembly of preformed crystalline TiO$_2$ nanoparticles, the resulting aerogels were reported to be amorphous, or only very few crystallites were found.[5,6,8,10,18]

The degree of crystallinity was determined with Rietveld refinement using an internal standard, which indicated significant crystalline content of TiO$_2$ anatase in the as-synthesized aerogel (Table 1). The degree of crystallinity of

Table 1. Rietveld Analysis of the Prepared TiO$_2$ Aerogel Samples

	TiO$_2$ crystalline phase/anatase wt %	TiO$_2$ amorphous phase wt %	crystallite size/nm
as-synthesized	10	90	4
300 °C	100	0	7
400 °C	100	0	10
500 °C	100	0	13

the as-synthesized TiO$_2$ aerogel could be due to the temperature and pressure during the supercritical drying process. It was reported by Moussaoui *et al.* that the drying conditions, such as high temperatures, can have an impact on the crystalline structure.[43] For calcination temperatures of 300−500 °C, the TiO$_2$ sample was completely crystallized, forming anatase.

The heat-treated TiO$_2$ aerogels at 300, 400, and 500 °C show reflections which can be assigned to the TiO$_2$ anatase crystal structure. No reflections can be assigned to the TiO$_2$ rutile crystal structure.[44]

According to the literature, anatase is the most likely occurring crystal structure at the applied calcination temperatures.[6] The anatase−rutile phase transition was reported to occur at temperatures between 400 and 800 °C.[3] The XRD pattern of the calcined aerogel at 500 °C exhibits well-defined and better-resolved reflections compared to the calcined aerogels at 300 and 400 °C, respectively. This indicates that the crystallinity increases with the calcination temperature. The crystallite sizes of the aerogels were estimated for the (101) reflection in the range of 23−28° 2θ. They increase with calcination temperature from 4 nm for the as-synthesized TiO$_2$ aerogel to 13 nm for the TiO$_2$ aerogel calcined at 500 °C (Table 1).

Figure S2 shows the Raman spectra of the TiO$_2$ aerogel. The Raman spectrum of the as-synthesized TiO$_2$ aerogel exhibits a broad band [E$_{g(1)}$ band] at 150.6 cm^{-1} and weak broad bands between 400 and 700 cm^{-1}. The heat-treated aerogels exhibit narrower Raman bands compared to the as-synthesized aerogel, which can be assigned clearly to anatase [141 cm^{-1} (E$_{g(1)}$), 197 cm^{-1} (E$_{g(2)}$), 398 cm^{-1} (B$_{1g(1)}$), 515 cm^{-1} (A$_{1g}$, B$_{1g(2)}$), and 640 cm^{-1} (E$_{g(3)}$)].[45−48] The bandwidth of the Raman bands decreases with increasing calcination temperature. The broad bands of the as-synthesized aerogels confirm the amorphous character of the sample. However, the bands found are more pronounced as reported in the literature for amorphous TiO$_2$ films.[49] This indicates a certain level of structural order of the material, which fits with the found crystallinity of 10 wt % in the as-synthesized aerogel sample. Also, Swamy *et al.* reported broad Raman bands for small crystallite sizes of 4 nm and narrow bands for crystallite sizes of 20 nm.[48] Thus, the nanosized crystals of 4 nm found for our as-synthesized aerogel and the low level of crystallinity could explain the broad but distinctive bands for the as-synthesized

aerogel sample. Kelly *et al.* report a band shift (blue shift) and band broadening for small crystallite sizes compared to large crystallize sizes.[47] This can be also seen for the herein synthesized TiO$_2$ aerogels. The maximum of the E$_{g(1)}$ bands shifts from 150.6 cm^{-1} of the as-synthesized aerogel to 141.3 cm^{-1} of the aerogel calcined at 500 °C, which fits with the literature values for crystalline anatase. A higher level of crystallinity leads to more pronounced Raman bands for the calcined TiO$_2$ aerogels compared to the semicrystalline as-synthesized aerogel.

The physisorption isotherms of the as-synthesized and heat-treated TiO$_2$ aerogels are presented in Figure 2. They exhibit a
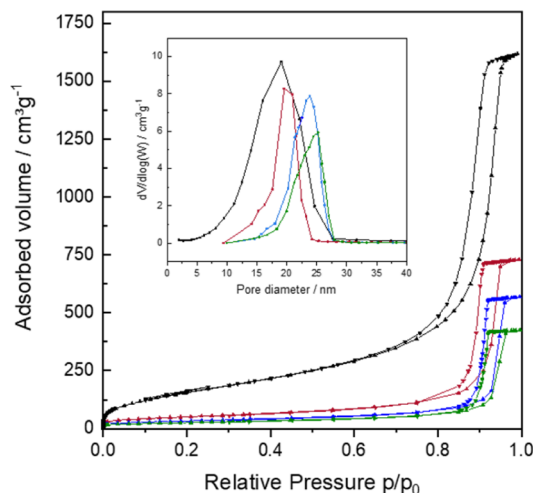
Figure 2. N$_2$ physisorption isotherms and BJH pore size distribution (inset) for the as-synthesized and heat-treated TiO$_2$ aerogels: as-synthesized TiO$_2$ aerogel (black) and aerogels calcined at 300 °C (red), 400 °C (blue), and 500 °C (green).

type IVa isotherm with the H1 hysteresis loop according to the IUPAC classifications, indicating a mesoporous material.[50] The desorption path is in thermodynamic equilibrium and different for the adsorption path, leading to hysteresis, which is associated with delayed capillary condensation during adsorption.[51,52] The type H1 hysteresis loop and the steep adsorption branch indicate a uniform and narrow pore size distribution. The adsorbed volume of nitrogen increases strongly at a relative pressure of $p/p^0 = 0.6$ for the as-synthesized TiO$_2$ aerogel before it reaches a plateau, indicating capillary condensation and saturation. For the heat-treated TiO$_2$ aerogels, the steep adsorption branch occurs at higher relative pressures, in particular, the higher the calcination temperature, the higher the relative pressure for the increase of adsorbed volume. This indicates larger pores after higher calcination temperatures. This is in good agreement with the pore size distribution shown in Figure 2 (inset).

A narrow pore size distribution was obtained for the as-synthesized and heat-treated TiO$_2$ aerogels. After heat treatment, the pore size distribution is slightly narrower, and the average pore size shifts to larger pore. This is in good agreement with the location of hysteresis loops, which occur at higher relative pressure and in a narrower pressure range for higher calcination temperatures. This can be explained by smaller mesopores (approx. 5−15 nm) which coalesced with larger mesopores (approx. 20 nm). The reduced number of smaller mesopores could also explain the decreased surface

area after heat treatment, as smaller pores contribute more to higher surface areas.[6]

The physisorption results are summarized in Table 2. The as-synthesized TiO$_2$ aerogel exhibits a high specific surface area

Table 2. Nitrogen Physisorption Results and Band Gaps of the Prepared TiO$_2$ Aerogel Samples

	BET surface area/m^2 g^{-1}	cumulative pore volume/cm^3 g^{-1}	average pore diameter/nm	band gap/eV
as-synthesized	600	2.5	19	3.5
300 °C	184	1.1	20	3.3
400 °C	118	0.9	24	3.3
500 °C	92	0.7	25	3.2

and a pore volume of 600 m^2 g^{-1} and 2.5 cm^3 g^{-1}, respectively. The supercritical drying process preserves the mesoporous structure of the as-synthesized TiO$_2$ aerogel, leading to the observed high values. Similar results have been reported in the literature by Sadrieyeh and Malekfar; however, the aging time could be reduced from >40 to 7 days during synthesis here, achieving a stable and translucent TiO$_2$ aerogel.[6] The specific surface area of the as-synthesized TiO$_2$ aerogel is in the same range as the reported literature values of 466 to 733 m^2 g^{-1} for amorphous TiO$_2$ aerogels, but it is semi-crystalline, which is not the case for the reported aerogels.[4,6−8] As expected, the surface area as well as the pore volume decrease for the heat-treated TiO$_2$ aerogel at 300 °C. The surface area and pore volume show a further decrease for the TiO$_2$ aerogels heat-treated at 400 and 500 °C, indicating a decrease in porosity. This is in accordance with the results reported in literature for calcined aerogel samples.[6] Even though the calcination of the TiO$_2$ aerogel reduced the specific surface area and porosity, both are higher compared to conventional bulk anatase and therefore is beneficial to use the investigated sol−gel synthesis conditions and supercritical drying for TiO$_2$ aerogel synthesis.[6] A comparable surface area of 85 m^2 g^{-1} was reported for an equally calcined TiO$_2$ aerogel by Lin *et al.*[19]

Figure 3 shows the SEM images of the TiO$_2$ aerogels at two different magnifications. The as-synthesized sample (a) shows mainly a smooth surface. The high-magnification SEM image (b) shows small, nearly spherical interconnected particles, which form an open porous network. This is highlighted with dotted lines in Figure 3b. Figure 3c−h shows the SEM images of the heat-treated TiO$_2$ aerogels at 300, 400, and 500 °C. The images show also a smooth uniform surface of the samples; however, the porosity of the samples decreases with higher calcination temperature, which is visible through the fewer and larger voids/pores between the particles and denser appearance of the microstructure. The particles become larger with higher calcination temperatures and seem to be arranged more densely.

In Figure 3d, small pores are still visible but have larger particles at 300 °C calcination temperature compared to the as-synthesized sample. Higher calcination temperatures lead to larger pores, and the denser microstructure becomes clearly visible at 400 °C calcination temperature, as seen in the highlighted areas in Figure 3f. The particle size increases further at 500 °C calcination temperature, which is highlighted in Figure 3h. These results are in good agreement with the N$_2$ physisorption results in Figure 2 and Table 2. The as-synthesized TiO$_2$ aerogel was further analyzed using TEM to confirm the observed semi-crystalline structure. Figure 4 shows
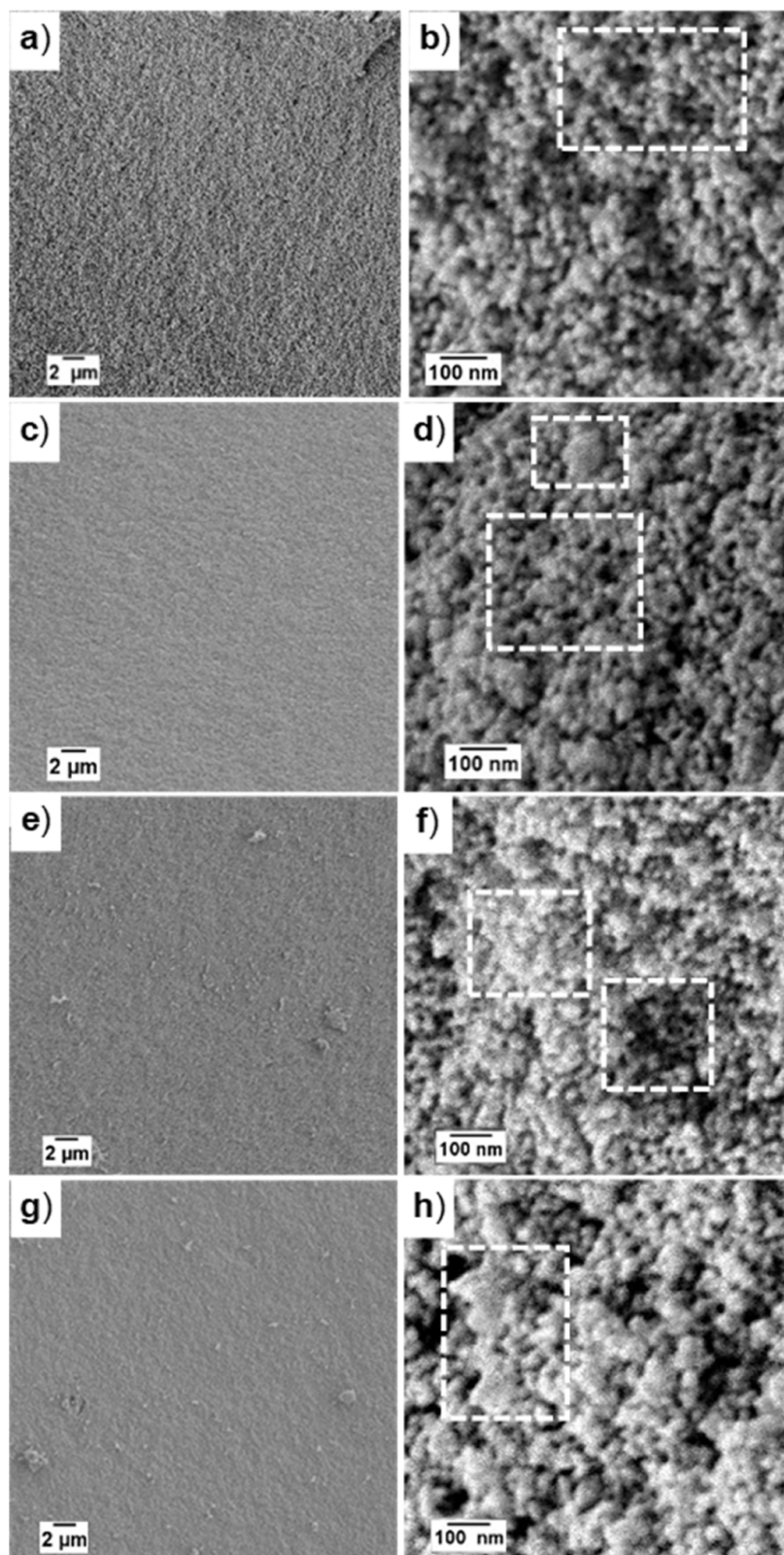
Figure 3. SEM images of the (a,b) as-synthesized aerogel, (c,d) calcined aerogel at 300 °C, (e,f) calcined aerogel at 400 °C, and (g,h) calcined aerogel at 500 °C at lower (5.000×) and higher (100.000×) magnifications.

the TEM images of the as-synthesized TiO_2 aerogel at different magnifications. Amorphous particles and nanocrystals can be observed. This is in good agreement with the XRD and Raman results shown in Figures 1 and S2, where a semi-crystalline structure was assumed. The TEM image shows the interconnected particles and nanocrystals in the porous network. It can be assumed that the particles in the aerogel network are connected by chemical means rather than by physical connection as in the P25 nanopowder. This is advantageous for photocatalytic hydrogen evolution, as this
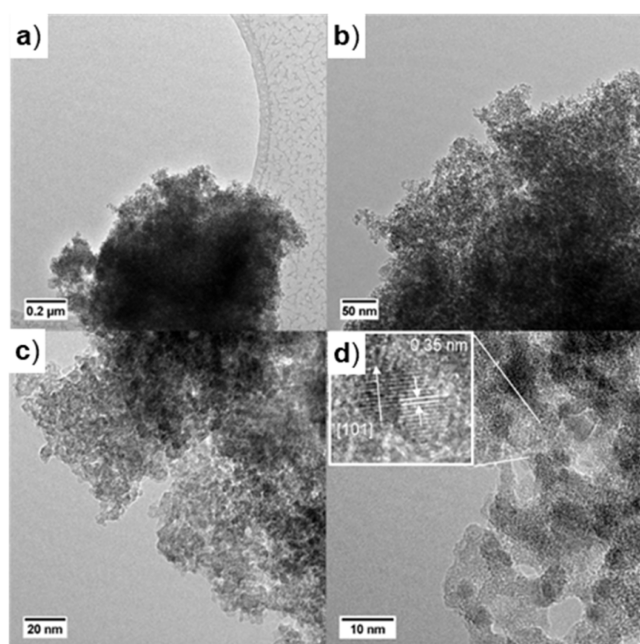
Figure 4. TEM images of as-synthesized TiO₂ aerogel: (a) 12.000×, (b) 39.000×, (c) 115.000×, and (d) 295.000×. The inset is a local enlargement of the TiO₂ nanocrystal.

Figure 5. Hydrogen evolution rates over time of the as-synthesized (black) and calcined TiO₂ aerogels at 300 °C (red), 400 °C (blue), and 500 °C (green); measured without cocatalyst for the first 100 min; measured with 0.0076 μmol m^{-2} Pt as the cocatalyst ($\triangleq$0.1 wt % for the as-synthesized sample) for approx. 30 min without irradiation. The photographs show the dispersions before irradiation and after 100 min of irradiation at 500, 400, and 300 °C and the as-synthesized sample from top to bottom.

could improve the separation of charge carriers. It was reported that the interconnected structure of TiO₂ nanocrystals offers better charge carrier delocalization compared to TiO₂ nanoparticle aggregates, for example, P25, which are physically connected.[53,54] The inset in Figure 4 shows the d-spacing, which was estimated to be 0.35 nm for the observed nanocrystals. This fits with the (101)-oriented anatase TiO₂ lattice plane and confirms the semi-crystalline nature of the as-synthesized TiO₂ aerogel.

The size of the nanocrystals was estimated approx. 4−6 nm, which is slightly larger compared to the calculated grain size from the XRD pattern (approx. 4 nm). This partial crystallinity was confirmed *via* Rietveld refinement. The amount of amorphous phase is decreased *via* heat treatment from the initial 10 wt % for the as-synthesized aerogel (Table 1) to none (within the boundaries of the error).

Absorption spectra in diffuse reflectance were recorded to characterize the optical properties of the TiO₂ aerogels. Diffuse reflectance spectra were converted to Kubelka−Munk spectra and Tauc plots for band gap estimation (Figure S3). Table 2 shows the estimated band gaps of the aerogel samples. The band gap of the as-synthesized TiO₂ aerogel is 3.5 eV, slightly higher than the band gap of the calcined aerogels of 3.2 to 3.3 eV, which was expected as it is a partially amorphous sample. The estimated band gaps are in correspondence with reported literature values for anatase TiO₂ powders and aerogels, with values ranging from 3.0 to 3.2 eV.[10,21,53,55] For all aerogels, only one sharp absorption edge at 340 to 375 nm is visible in the UV−vis spectra, indicating that no biphases are formed.

3.2. Photocatalytic Electron Storage and Hydrogen Generation. Photocatalytic experiments were performed with all TiO₂ aerogel samples to investigate the influence of the physicochemical properties of the aerogels on the electron storage capability and photocatalytic activity (Figure 5). For this, 100 mg of the aerogel was dispersed in 150 mL of a 2.5
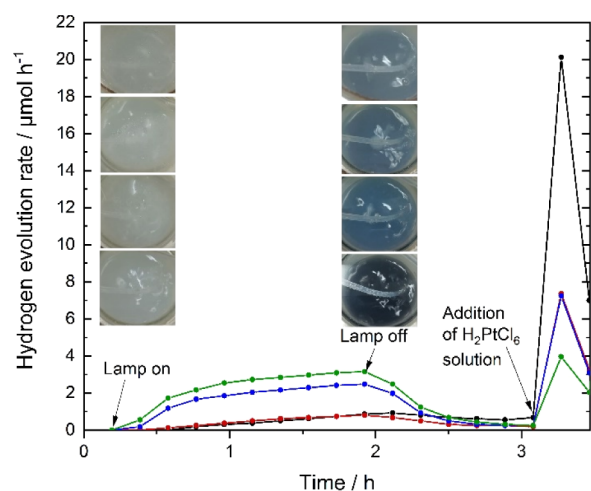
mol L^{-1} aqueous methanol solution and irradiated with a 300 W Xe lamp (see Experimental Section). The samples were first irradiated for 100 min without a cocatalyst. Then, the lamp was turned off to show that the hydrogen evolution is really a photocatalytic effect, as indicated by a decrease in the hydrogen evolution rate as no more charge carriers are generated. The simultaneous color change of the dispersions is shown in Figure 5 as well, changing from a colorless dispersion to a blueish-colored dispersion after irradiation. Enlarged versions of the photographs are given additionally in the Supporting Information (Figure S4). This blue coloration is an indication of the storage of electrons and formation of Ti^{3+} states.[26,28,30,56] Their recombination is inhibited due to the use of methanol as a hole scavenger, reacting fast with photogenerated holes.[25]

The intensity of the blue color decreases with increasing calcination temperature of the aerogels and, therefore, also with the surface area of the TiO₂ aerogel samples. Meanwhile, the amounts of detected hydrogen are very low (below 10 μmol h^{-1}), as expected for unmodified TiO₂. Indeed, the sample with the smallest surface area—calcined at 500 °C— offers the best hydrogen evolution rate up to 3.2 μmol h^{-1}. This hydrogen evolution rate is higher than reported hydrogen evolution rates of ∼1 μmol h^{-1} for a comparable calcined sample with 85 m^2 g^{-1} surface area measured at even higher temperatures of 30 °C.[19] It can be assumed that, besides the improved crystallinity confirmed by XRD, the interconnection of the TiO₂ nanocrystals in the aerogels improves with higher calcination temperatures, which is advantageous for the photocatalytic hydrogen production, as the charge carrier separation seems to be improved. This finding is comparable to results of Amal *et al.* on WO₃ photoelectrodes, where a higher calcination temperature led to improved crystallinity, better charge transportation (lower electron storage), and therefore higher photocatalytic H₂ evolution.[37] The heat treatment can also reduce the amount of bulk defects, which are recombination centers. Kong *et al.* reported a reduced bulk

to surface defect ratio and increased photocatalytic activity for TiO_2 nanocrystals, which were calcined compared to TiO_2 nanocrystals, which were prepared without a calcination step.[57]

After the lamp was switched off and the hydrogen evolution went to zero (since no more charge carriers are generated), an aqueous H_2PtCl_6 solution was added to the bluish dispersions *via* rubber sealing (to keep the inert atmosphere in the reactor), to achieve Pt decoration *via* subsequent photodeposition. However, even without light irradiation, a few seconds after the addition of the cocatalyst precursor solution, the coloration of the dispersion disappeared. At the same time, a sharp peak in the hydrogen evolution rate was detected in all four cases even without light irradiation (sharp peak after 3 h in Figure 5). The intensity of this hydrogen evolution peak without light irradiation has the same trend as the intensity of the blueish color of the dispersion: The darker the dispersion before H_2PtCl_6 addition, the higher the hydrogen evolution peak after the addition, up to 20 μmol h^{-1} if a gas chromatograph is used for the detection of hydrogen every ~11 min.

This hydrogen evolution rate peak can be explained by the photogenerated and stored electrons in the aerogel sample being used to form metallic Pt clusters on the TiO_2 aerogels upon H_2PtCl_6 reduction. After all Pt ions are reduced, forming Pt metal nanoparticles on TiO_2, a Schottky contact is formed between Pt and TiO_2, upon which the excess of stored electrons in the aerogels are transferred to the Pt metal particles, where they are used to reduce protons to hydrogen, acting as cocatalysts. This hydrogen is then detected as the sharp peak in the hydrogen evolution rate curve. This kind of mechanism was already reported before for different metal cocatalyst deposition on TiO_2.[26,27,56,58] The intensity of this peak is therefore—beneath the intensity of the blue color—an indication for the amount of stored electrons. Furube *et al.* reported an improved charge carrier separation by Pt deposition on TiO_2 by use of transient absorption spectroscopy, which additionally explains the enhancement of hydrogen evolution rate.[59]

The electron storage capability of the aerogels can be related to their physicochemical properties. The as-synthesized, partially amorphous sample with the highest surface area can store the most electrons, as indicated by the most intense blue coloration. Ikeda *et al.* reported that electrons are trapped at defective sites in TiO_2 for example, oxygen vacancies, which are mainly located at the surface of TiO_2. They state that the quantity of accumulated electrons represents the number of defective sites.[60] The as-synthesized aerogel can therefore store the most photocharged electrons due to the highest surface area and presumably highest amount of surface defects, due to its low heat treatment. An increase in the heat treatment and decrease in surface area results in a decreased amount of stored electrons.

In the case of the semi-crystalline as-synthesized TiO_2 aerogel, more electrons are stored in the material and are not used for the hydrogen evolution under light irradiation, as can be seen in the coloration of the dispersion. This is an indication that the electrons are trapped in surface defects and not in bulk defects, where electrons would recombine with holes. Surface defects are on the one hand charge carrier traps and on the other hand adsorption sites for methanol as a hole scavenger.[57] Electrons are trapped, and recombination is prevented by the fast and efficient reaction of the holes with methanol, which makes the untreated aerogel the best electron

storage material in this study. Heat treatment seems to reduce the amount of surface defects and bulk defects leading to reduced electron storage, but improved charge carrier separation and hydrogen evolution.

The dependence on the heat treatment of the aerogel can be seen also in the photocatalytic hydrogen evolution rates after cocatalyst deposition (Table 3). After the deposition of the

Table 3. Hydrogen Evolution Rates of the Prepared TiO_2 Aerogel Samples

	hydrogen evolution rate (with 0.1 wt % Pt)/μmol h^{-1}
as-synthesized	25.5
300 °C	176.5
400 °C	279.2
500 °C	331.8

cocatalyst, no blue coloration of the dispersion can be observed anymore (Figure S2), as the electrons are transferred to the formed metallic Pt particles, where they are used for the hydrogen evolution and not stored in the material. All samples exhibit the same amount of cocatalyst, nevertheless a clear difference in the activity is observed. As the Pt particles prevent the storage of the electrons in surface defect states, the difference in the activity can be explained by the heat treatment and the amount of bulk defects. The heat-treated aerogels show decreased charge carrier recombination and therefore higher activity compared to the semi-crystalline aerogel. This can be explained by the decreased number of surface and bulk defects due to the calcination process as well as the photocatalytic activity of exposed facets of the crystalline phase.[61] The photocatalytic activity is also improved by the sintered and chemically linked TiO_2 nanoparticles, due to the wide distribution and therefore better separation of charge carriers, up to 340 μmol h^{-1} for the aerogel calcined at 500 °C (Table 3).[19] Taking the low amount of cocatalyst loading with 0.1 wt % into account, this hydrogen evolution rate is quite high compared to hydrogen evolution rates of 16.4 μmol h^{-1} at 30 °C for a 0.5 wt % Pt-loaded TiO_2 aerogel or 720 μmol h^{-1} for 1 wt % loaded TiO_2 aerogel.[19,21]

The TiO_2 aerogels were all regained after the photocatalytic hydrogen evolution experiments by washing and supercritical drying. The XRD pattern after the photocatalytic hydrogen production experiments is shown in Figure S5. The XRD pattern of the heat-treated aerogels shows no changes, and reflections from the small amounts of Pt added are not visible. Interestingly, the as-synthesized aerogel sample exhibits more pronounced reflections than before the experiments but still offers a semi-crystalline character. Rietveld refinement indicated an increase in crystallinity of the as-synthesized TiO_2 aerogel after UV irradiation/photocatalytic hydrogen experiment from approx. 10 to 40 wt % crystalline content. Zywitzki *et al.* already showed that amorphous TiO_2 can be prepared by an UV-light-mediated synthesis using Ti(OEt)$_4$ as an titanium alkoxide precursor. The increase of crystallinity of the as-synthesized aerogel after UV-light exposure could be related to UV irradiation with the Xe lamp used in the experiment. This will be further investigated in future studies.[56]

Commercial anatase nanoparticles were measured in comparison to the as-synthesized TiO_2 aerogel to show the benefit of the aerogel prepared in the present work (Figure S6). The as-synthesized aerogel exhibits better electron storage ability, as shown by the intense coloration, compared to

commercial anatase nanoparticles. The coloration of the commercial anatase nanoparticles is comparable to the coloration of the calcined aerogels. The BET surface area and XRD of the commercial anatase was also measured for comparison. The determined BET surface area is 311 m^2 g^{-1}. The XRD pattern is comparable to the 300 °C calcined aerogel sample, with a comparable crystallite size (Figure S7).

We showed that the material properties of the aerogels have a direct influence on their electron storage capability. To verify the differences in the amount of stored electrons in the aerogel samples, quantification of the stored electrons was performed *via* the reduction reaction of Pt^{4+} to Pt^0 in the dark with high-resolution detection of the evolved hydrogen evolution peak, with a mass spectrometer every 13 s. Pt is one of the best candidates for this since the large work function of Pt (low Fermi level) forces the electrons to be transferred to Pt (trapping of electrons) as a Schottky contact between Pt and TiO$_2$ is formed.[62] Furthermore, Pt shows the lowest activation energy for H$_2$ evolution. Therefore, Pt was chosen for the experiments in the dark.[63] Figure 6 shows the hydrogen
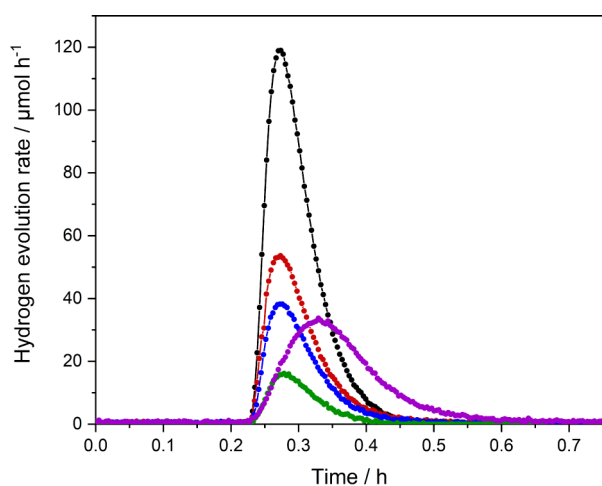
Figure 6. Hydrogen evolution rates in the dark for the quantification of stored electrons in the as-synthesized (black) TiO$_2$ aerogel and aerogels calcined at 300 °C (red), 400 °C (blue), and 500 °C (green) and in commercial anatase (purple) for comparison. The samples were irradiated for 100 min, and it was left to rest until H$_2$ evolution was 0 μmol h^{-1} (this time was set to 0 h here), for a stable baseline for curve integration. Then, Pt solution was added after 0.2 h to reach 0.1 wt %, and the hydrogen evolution was measured until no evolution was detected anymore.

evolution peak after addition of 0.1 wt % Pt to the dispersed aerogel samples irradiated for 100 min. Additionally, the quantification was done for the commercial anatase nanoparticles for comparison. For this investigation, we make the viable assumption that all Pt^{4+} is reduced to Pt^0 and that the remaining stored electrons are used only for the hydrogen evolution reaction; no other reaction partners are present. Thus, the amount of stored electrons can be quantified.

As the amount of added Pt solution is for all samples the same, the amount of stored electrons needed for the reduction of Pt^{4+} to Pt^0 is for all samples 2 μmol. The amount of evolved hydrogen differs, depending on the amount of stored electrons.

As expected, the dark hydrogen evolution of the as-synthesized aerogel in Figure 6 is the highest in comparison to the calcined aerogels and to the commercial anatase nanoparticles and decreases with the calcination temperature. This fits with the intensity of blue coloration—the amount of Ti^{3+}—in the photographs in Figure 5, which decreases with increasing calcination temperature.
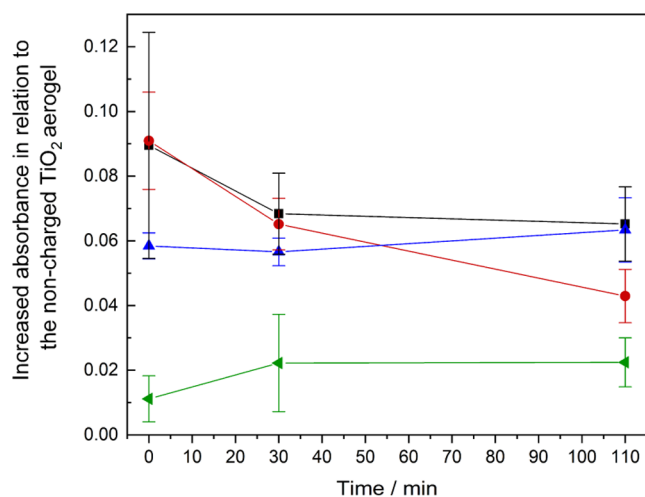
By integration of the hydrogen evolution rate transient, the amount of electrons can be quantified. Two electrons are needed to evolve one molecule of hydrogen. Table 4 shows the result of the quantification experiments. The sum of the electrons used for the reduction of Pt^{4+} to Pt^0 and the hydrogen evolution equals the amount of stored electrons in the sample. The amount of stored electrons is 22.0 μmol for the as-synthesized aerogel and becomes lower from 11.6 μmol down to 4.8 μmol for the calcined aerogels. The commercial anatase nanoparticles store 13.0 μmol of electrons, which in the same range as for the 300 °C calcined aerogel. The difference in the surface area—311 m^2 g^{-1} compared to 184 m^2 g^{-1} for the aerogel—does not have such a high influence on the electron storage ability compared to the aerogel samples. Here, the different preparation conditions of the commercial anatase sample have to be taken into account when comparing the commercial anatase nanoparticles with the aerogel samples. It seems that the crystallinity has a stronger influence on the electron storage ability of the commercial anatase than it does for the aerogel, where the surface area has the prominent effect on the electron storage ability. The dependency of the electron storage ability on the crystallinity was shown before for WO$_3$ electrodes.[37] Compared to the commercial anatase nanoparticles, the as-synthesized aerogel stores 1.7 times more electrons. As expected, the aerogel calcined at 500 °C stores the smallest amount of electrons with 4.8 μmol—0.22 times that of the as-synthesized aerogel—but shows the highest hydrogen evolution activity in the hydrogen evolution experiments with 4 times that of the as-synthesized aerogel without a cocatalyst.

The percentage of Ti^{3+} states—presumably the amount of stored electrons—formed in 100 mg of TiO$_2$ aerogels and commercial anatase nanoparticles was also calculated (Table 4) and ranges from 0.4% for the calcined aerogel at 500 °C to 1.8% for the as-synthesized aerogel. The percentage of Ti^{3+} formed in the commercial anatase nanoparticles is 1.0%.

Table 4. Amount of Stored Electrons Quantified by the Reduction of Pt^{4+} to Pt^0 in the Dark and Measurement of Evolved H$_2$ and Percentage of Ti^{3+} States after Charging for 100 min

	amount of electrons by Pt^{4+} reduction (0.1 wt %)/μmol	amount of electrons from H$_2$ evolution/μmol	sum of amount of electrons from Pt^{4+} reduction and H$_2$ evolution/μmol	percentage of Ti^{3+} states after charging/%
as-synthesized	2	20.0	22.0	1.8
300 °C	2	9.6	11.6	0.9
400 °C	2	7.1	9.1	0.7
500 °C	2	2.8	4.8	0.4
commercial anatase	2	11.0	13.0	1.0

Additionally, to the quantification of electrons, the absorbance of the aerogel dispersions was measured in the range between 350 and 800 nm before and after irradiation of the experiment, as shown in Figure 5. To detect the time-dependent fading in the absorbance of the dispersions, the absorbance was determined immediately after the irradiation for 100 min, 30 min after irradiation was stopped, and 110 min after irradiation was stopped (Figure S8). For this test, dispersions of 100 mg of the TiO$_2$ aerogel in 150 mL of a 2.5 mol L^{-1} aqueous methanol solution were irradiated. The increase in absorption of the dispersions after irradiation for 100 min (charging) was detected at a wavelength of 600 nm and compared to the absorbance of the dispersions before irradiation (Figure 7). The absorbance increase directly after

irradiated for 100 min while simultaneously hydrogen evolution was detected. Additionally, photographs of the dispersions were taken directly after the irradiation (Figure 8),

Figure 8. Hydrogen evolution rates over time of the as-synthesized TiO$_2$ aerogel dispersed in aqueous methanol solutions with different methanol concentrations plus photographs of the dispersions after an irradiation time of 100 min. Irradiation was stopped after 100 min.

Figure 7. Absorption changes measured after charging of as-synthesized (black) TiO$_2$ aerogels and TiO$_2$ aerogels calcined at 300 °C (red), 400 °C (blue), and 500 °C (green) (top). The increase in absorbance at 600 nm after 100 min irradiation (charging, = 0 min) is given, followed by two additional measurements (30 and 110 min after irradiation, respectively) without irradiation, indicating color fading (bottom).

irradiation for 100 min is most prominent in the as-synthesized aerogel and the aerogel calcined at 300 °C, being lower for higher calcination temperatures of the aerogel. This is in good agreement with the photographs taken and shown in Figure 5. A decay in absorbance increase after irradiation is most prominent for the sample calcined at 300 °C and also detectable for the as-synthesized aerogel. For calcined samples at higher temperatures, hardly any decay of the absorption increase is detectable in the investigated time range. The decay in the absorbance is attributable to a decreasing amount of stored electrons in the aerogel sample, which can be due to either charge carrier recombination or reduction reaction. Electron storage is preferred in aerogel samples with lower heat treatment, which goes directly in line with reduced rates for photocatalytic hydrogen evolution, in accordance with the photocatalysis results.

Since the results led to the conclusion that the as-synthesized aerogel seems to offer the best electron storage ability, further experiments were performed with this sample. The influence of the methanol concentration on electron storage was additionally tested. Dispersions of 100 mg of the aerogel in 150 mL aqueous solution with different methanol concentrations ranging from 0.02 up to 19.7 mol L^{-1} were
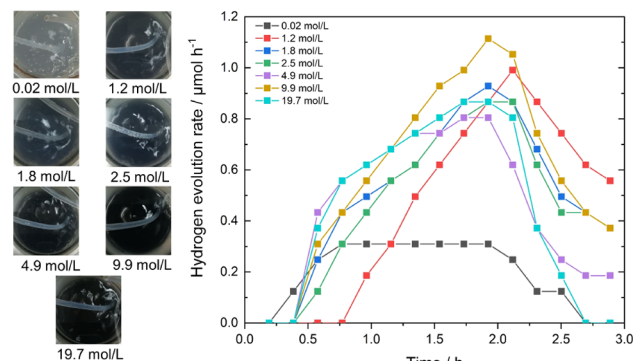
enlarged versions of the photographs are given in the Supporting Information (Figure S9). All dispersions show the typical blue coloration as an indication of the storage of electrons and formation of Ti^{3+} states. Only a very slight coloration and presumably a small amount of stored electrons are visible for the lowest methanol concentration of 0.02 mol L^{-1} after irradiation for 100 min. This goes in line with the negligible amount of evolved hydrogen. For all other methanol concentrations higher than 0.02 mol L^{-1}, a comparable hydrogen evolution rate between 0.8 and 1.1 μmol h^{-1} is detected. The higher the methanol concentration is, the darker the coloration of the dispersion after the same time of irradiation. Thus, the amount of stored electrons can be adjusted by the used methanol concentration. The higher the concentration of the hole scavenger, the higher is the amount of stored electrons, but hardly any changes in hydrogen evolution rates are observed. From these results, it can be concluded that, in the case of very small amounts of hole scavenger, the recombination rate at the surface defects is increased as the holes cannot react with methanol before recombining with trapped electrons. The higher the concentration of the hole scavenger, the more methanol can adsorb on surface defects, and the charge carrier recombination is strongly reduced, which is visible in an increased coloration of the dispersion, indicating an increased number of stored electrons and therefore Ti^{3+} states in the sample. This further supports the results from the hydrogen evolution experiments. These results pave the way for future hydrogen-on-demand applications, when charging and hydrogen evolution can be spatially and timely separated.

A material like the presented as-synthesized TiO$_2$ aerogel with high electron storage ability and a high amount of surface defects offers the possibility for applying it for other redox reactions, for example, in dark reduction reactions of very stable molecules. One of the currently most investigated reactions of this type is the nitrogen reduction reaction.[64,65] Surface oxygen vacancies can be beneficial for the N$_2$ adsorption and conversion, which makes the as-synthesized TiO$_2$ aerogel an interesting material in this research area.[66] Furthermore, Bahnemann et al. showed in 2011 that photoexcited electrons stored in TiO$_2$ colloids can reduce

J

N₂.[25] Therefore, a similar experiment with the as-synthesized TiO_2 aerogel was performed. 100 mg of the as-synthesized aerogel sample was dispersed in 150 mL of an aqueous 2.5 mol L^{-1} methanol solution and irradiated for 100 min under argon to store electrons in the sample. Subsequently, the lamp was turned off, and the gas flow was switched to nitrogen, flushing through the dispersion for 7 h. Afterward, a salicylate test was performed to determine the amount of produced ammonia. Figure S10 shows the absorbance spectra of this salicylate test. An absorbance peak is visible after the reaction time of 7 h (no signal without N₂), which relates to an obtained ammonia yield of 5 μg L^{-1}. This positive test for a dark nitrogen reduction reaction with stored photogenerated electrons on an as-synthesized TiO_2 aerogel sample gives rise to future research work on such aerogels for photocatalytic ammonia generation, in which the mechanism for this dark reaction will be investigated, too. Nevertheless, it opens up possibilities to optimize reaction conditions for the charging process and the dark reduction reaction separately in the future.

4. CONCLUSIONS

Mesoporous TiO_2 aerogels with large surface areas were prepared *via* acid-catalyzed sol−gel synthesis and supercritical drying. As-synthesized TiO_2 aerogels and TiO_2 aerogels calcined at 300, 400, and 500 °C exhibit surface areas of 600, 184, 118, and 92 m^2 g^{-1}, respectively. Interestingly, even without calcination, the as-synthesized aerogel is partly crystalline with anatase crystallites.

TiO_2 aerogels are able to store large amounts of photogenerated electrons in surface trap states upon illumination in water−methanol dispersions. The capacity to store photogenerated electrons increases at lower calcination temperatures. Furthermore, the extent of electron storage also depends on the methanol scavenger concentration. The amount of stored electrons for a constant methanol concentration was quantified by Pt^{4+} reduction and showed a maximum amount of stored electrons of 22 μmol for the as-synthesized TiO_2 aerogel. The as-synthesized aerogel stores 1.7 times more electrons than commercial anatase nanoparticles. Increasing the calcination temperature to 500 °C results in a decreased surface area but strongly increased hydrogen evolution rates in photocatalytic experiments.

Finally, nitrogen reduction to ammonia in the dark was performed with photogenerated stored electrons in TiO_2 aerogels, separating the charge carrier photogeneration from the nitrogen reduction reaction. This result paves the way for future application of such tailored and cheap TiO_2 aerogels in solar fuel-on-demand processes.

■ ASSOCIATED CONTENT

Ⓢ🔵 Supporting Information

The Supporting Information is available free of charge at https://pubs.acs.org/doi/10.1021/acsaem.2c02517.

> Lamp spectra of the light source, Raman spectra, Kubelka−Munk spectra, additional enlarged photographs of photocharged dispersions, postcatalytic XRD data, XRD data of commercial TiO_2, absorption spectra of photocharged dispersions, and salicylate test results (PDF)

■ AUTHOR INFORMATION

Corresponding Author

Roland Marschall − *Department of Chemistry, University of Bayreuth, Bayreuth 95447, Germany;* 🔵 orcid.org/0000-0002-1057-0459; Email: roland.marschall@uni-bayreuth.de

Authors

Alexandra Rose − *German Aerospace Center, Institute of Materials Research, Aerogels and Aerogel Composites, Köln 51147, Germany*

Anja Hofmann − *Department of Chemistry, University of Bayreuth, Bayreuth 95447, Germany*

Pascal Voepel − *German Aerospace Center, Institute of Materials Research, Aerogels and Aerogel Composites, Köln 51147, Germany*

Barbara Milow − *German Aerospace Center, Institute of Materials Research, Aerogels and Aerogel Composites, Köln 51147, Germany*

Complete contact information is available at:
https://pubs.acs.org/10.1021/acsaem.2c02517

Author Contributions

The manuscript was written through contributions of all authors. All authors have given approval to the final version of the manuscript. A.R. and A.H. contributed equally.

Notes

The authors declare no competing financial interest.

■ REFERENCES

(1) Hüsing, N.; Schubert, U. Aerogels-Airy Materials: Chemistry, Structure, and Properties. *Angew. Chem. Int. Ed.* **1998**, 37, 22−45.

(2) Alwin, S.; Sahaya Shajan, X. Aerogels: Promising Nanostructured Materials for Energy Conversion and Storage Applications. *Mater Renew Sustain Energy* **2020**, 9, 7.

(3) Song, K. C.; Pratsinis, S. E. Control of Phase and Pore Structure of Titania Powders Using HCl and NH₄OH Catalysts. *J. Am. Ceram. Soc.* **2001**, 84, 92−98.

(4) Choi, H.; Carboni, M.; Kim, Y. K.; Jung, C. H.; Moon, S. Y.; Koebel, M. M.; Park, J. Y. Synthesis of High Surface Area TiO2 Aerogel Support with Pt Nanoparticle Catalyst and CO Oxidation Study. *Catal. Lett.* **2018**, 148, 1504−1513.

(5) Schäfer, H.; Milow, B.; Ratke, L. Synthesis of Inorganic Aerogels via Rapid Gelation Using Chloride Precursors. *RSC Adv.* **2013**, 3, 15263−15272.

(6) Sadrieyeh, S.; Malekfar, R. The Effects of Hydrolysis Level on Structural Properties of Titania Aerogels. *J. Non-Cryst. Solids* **2017**, 457, 175−179.

(7) Schäfer, H.; Milow, B.; Ratke, L. Synthesis of Inorganic Aerogels via Rapid Gelation Using Chloride Precursors. *RSC Adv.* **2013**, 3, 15263.

(8) Lermontov, S. A.; Straumal, E. A.; Mazilkin, A. A.; Baranchikov, A. E.; Straumal, B. B.; Ivanov, V. K. An Approach for Highly

Transparent Titania Aerogels Preparation. *Mater. Lett.* **2018**, *215*, 19−22.

(9) Anderson, M. L.; Stroud, R. M.; Morris, C. A.; Merzbacher, C. I.; Rolison, D. R. Tailoring Advanced Nanoscale Materials through Synthesis of Composite Aerogel Architectures. *Adv. Eng. Mater.* **2000**, *2*, 481−488.

(10) Luna, A. L.; Matter, F.; Schreck, M.; Wohlwend, J.; Tervoort, E.; Colbeau-Justin, C.; Niederberger, M. Monolithic Metal-Containing TiO2 Aerogels Assembled from Crystalline Pre-Formed Nanoparticles as Efficient Photocatalysts for H2 Generation. *Appl. Catal., B* **2020**, *267*, 118660.

(11) Parale, V. G.; Kim, T.; Phadtare, V. D.; Yadav, H. M.; Park, H. H. Enhanced Photocatalytic Activity of a Mesoporous TiO2 Aerogel Decorated onto Three-Dimensional Carbon Foam. *J. Mol. Liq.* **2019**, *277*, 424−433.

(12) Kim, T.; Parale, V.; Jung, H.-N.-R.; Kim, Y.; Driss, Z.; Driss, D.; Bouabidi, A.; Euchy, S.; Park, H.-H. Facile Synthesis of SnO2 Aerogel/Reduced Graphene Oxide Nanocomposites via in Situ Annealing for the Photocatalytic Degradation of Methyl Orange. *Nanomaterials* **2019**, *9*, 358.

(13) Parale, V. G.; Kim, T.; Lee, K. Y.; Phadtare, V. D.; Dhavale, R. P.; Jung, H. N. R.; Park, H. H. Hydrophobic TiO2−SiO2 Composite Aerogels Synthesized via in Situ Epoxy-Ring Opening Polymerization and Sol-Gel Process for Enhanced Degradation Activity. *Ceram. Int.* **2020**, *46*, 4939−4946.

(14) Bernardes, J. C.; Pinheiro, G. K.; Muller, D.; Latocheski, E.; Domingos, J. B.; Rambo, C. R. Novel Modified Nonalkoxide Sol−gel Synthesis of Multiphase High Surface Area TiO2 Aerogels for Photocatalysis. *J. Sol-Gel Sci. Technol.* **2020**, *94*, 425−434.

(15) DeSario, P. A.; Pietron, J. J.; Taffa, D. H.; Compton, R.; Schünemann, S.; Marschall, R.; Brintlinger, T. H.; Stroud, R. M.; Wark, M.; Owrutsky, J. C.; Rolison, D. R. Correlating Changes in Electron Lifetime and Mobility on Photocatalytic Activity at Network-Modified TiO2 Aerogels. *J. Phys. Chem. C* **2015**, *119*, 17529−17538.

(16) Panayotov, D. A.; DeSario, P. A.; Pietron, J. J.; Brintlinger, T. H.; Szymczak, L. C.; Rolison, D. R.; Morris, J. R. Ultraviolet and Visible Photochemistry of Methanol at 3D Mesoporous Networks: TiO2 and Au−TiO2. *J. Phys. Chem. C* **2013**, *117*, 15035−15049.

(17) Parayil, S. K.; Psota, R. J.; Koodali, R. T. Modulating the Textural Properties and Photocatalytic Hydrogen Production Activity of TiO2 by High Temperature Supercritical Drying. *Int. J. Hydrogen Energy* **2013**, *38*, 10215−10225.

(18) Kwon, J.; Choi, K.; Schreck, M.; Liu, T.; Tervoort, E.; Niederberger, M. Gas-Phase Nitrogen Doping of Monolithic TiO2nanoparticle-Based Aerogels for Efficient Visible Light-Driven Photocatalytic H2production. *ACS Appl. Mater. Interfaces* **2021**, *13*, 53691−53701.

(19) Lin, C.-C.; Wei, T.-Y.; Lee, K.-T.; Lu, S.-Y. Titania and Pt/titania Aerogels as Superior Mesoporous Structures for Photocatalytic Water Splitting. *J. Mater. Chem.* **2011**, *21*, 12668.

(20) Puskelova, J.; Baia, L.; Vulpoi, A.; Baia, M.; Antoniadou, M.; Dracopoulos, V.; Stathatos, E.; Gabor, K.; Pap, Z.; Danciu, V.; Lianos, P. Photocatalytic Hydrogen Production Using TiO2-Pt Aerogels. *Chem. Eng. J.* **2014**, *242*, 96−101.

(21) Puskelova, J.; Baia, L.; Vulpoi, A.; Baia, M.; Antoniadou, M.; Dracopoulos, V.; Stathatos, E.; Gabor, K.; Pap, Z.; Danciu, V.; Lianos, P. Photocatalytic Hydrogen Production Using TiO2−Pt Aerogels. *Chem. Eng. J.* **2014**, *242*, 96−101.

(22) Di Iorio, Y.; Aguirre, M. E.; Brusa, M. A.; Grela, M. A. Surface Chemistry Determines Electron Storage Capabilities in Alcoholic Sols of Titanium Dioxide Nanoparticles. A Combined FTIR and Room Temperature EPR Investigation. *J. Phys. Chem. C* **2012**, *116*, 9646−9652.

(23) Panayotov, D. A.; DeSario, P. A.; Pietron, J. J.; Brintlinger, T. H.; Szymczak, L. C.; Rolison, D. R.; Morris, J. R. Ultraviolet and Visible Photochemistry of Methanol at 3D Mesoporous Networks: TiO2 and Au-TiO2. *J. Phys. Chem. C* **2013**, *117*, 15035−15049.

(24) Sachs, M.; Pastor, E.; Kafizas, A.; Durrant, J. R. Evaluation of Surface State Mediated Charge Recombination in Anatase and Rutile TiO2. *J. Phys. Chem. Lett.* **2016**, *7*, 3742−3746.

(25) Bahnemann, D.; Henglein, A.; Lilie, J.; Spanhel, L. Flash Photolysis Observation of the Absorption Spectra of Trapped Positive Holes and Electrons in Colloidal Titanium Dioxide. *J. Phys. Chem.* **1984**, *88*, 709−711.

(26) Mohamed, H. H.; Dillert, R.; Bahnemann, D. W. Growth and Reactivity of Silver Nanoparticles on the Surface of TiO 2: A Stopped-Flow Study. *J. Phys. Chem. C* **2011**, *115*, 12163−12172.

(27) Mohamed, H. H.; Dillert, R.; Bahnemann, D. W. Kinetic and Mechanistic Investigations of the Light Induced Formation of Gold Nanoparticles on the Surface of TiO2. *Chem. Eur J.* **2012**, *18*, 4314−4321.

(28) Mohamed, H. H.; Dillert, R.; Bahnemann, D. W. Reaction Dynamics of the Transfer of Stored Electrons on TiO2 Nanoparticles: A Stopped Flow Study. *J. Photochem. Photobiol., A* **2011**, *217*, 271−274.

(29) Mohamed, H. H.; Dillert, R.; Bahnemann, D. W. TiO2 Nanoparticles as Electron Pools: Single- and Multi-Step Electron Transfer Processes. *J. Photochem. Photobiol., A* **2012**, *245*, 9−17.

(30) Mohamed, H. H.; Mendive, C. B.; Dillert, R.; Bahnemann, D. W. Kinetic and Mechanistic Investigations of Multielectron Transfer Reactions Induced by Stored Electrons in TiO2 Nanoparticles: A Stopped Flow Study. *J. Phys. Chem. A* **2011**, *115*, 2139−2147.

(31) Sakar, M.; Nguyen, C. C.; Vu, M. H.; Do, T. O. Materials and Mechanisms of Photo-Assisted Chemical Reactions under Light and Dark Conditions: Can Day−Night Photocatalysis Be Achieved? *ChemSusChem* **2018**, *11*, 809−820.

(32) Ng, C.; Ng, Y. H.; Iwase, A.; Amal, R. Visible Light-Induced Charge Storage, on-Demand Release and Self-Photorechargeability of WO3 Film. *Phys. Chem. Chem. Phys.* **2011**, *13*, 13421−13426.

(33) Ng, C.; Iwase, A.; Ng, Y. H.; Amal, R. Understanding Self-Photorechargeability of WO3 for H2 Generation without Light Illumination. *ChemSusChem* **2013**, *6*, 291−298.

(34) Schulz, M.; Hagmeyer, N.; Wehmeyer, F.; Lowe, G.; Rosenkranz, M.; Seidler, B.; Popov, A.; Streb, C.; Vos, J. G.; Dietzek, B. Photoinduced Charge Accumulation and Prolonged Multielectron Storage for the Separation of Light and Dark Reaction. *J. Am. Chem. Soc.* **2020**, *142*, 15722−15728.

(35) Lau, V. W.; Lotsch, B. V. A Tour-Guide through Carbon Nitride-Land: Structure- and Dimensionality-Dependent Properties for Photo(Electro)Chemical Energy Conversion and Storage. *Adv. Energy Mater.* **2021**, *12*, 2101078.

(36) Kröger, J.; Jiménez-Solano, A.; Savasci, G.; Rovó, P.; Moudrakovski, I.; Küster, K.; Schlomberg, H.; Vignolo-González, H. A.; Duppel, V.; Grunenberg, L.; Dayan, C. B.; Sitti, M.; Podjaski, F.; Ochsenfeld, C.; Lotsch, B. V. Interfacial Engineering for Improved Photocatalysis in a Charge Storing 2D Carbon Nitride: Melamine Functionalized Poly(heptazine Imide). *Adv. Energy Mater.* **2021**, *11*, 2003016.

(37) Ng, C.; Ng, Y. H.; Iwase, A.; Amal, R. Influence of Annealing Temperature of WO3 in Photoelectrochemical Conversion and Energy Storage for Water Splitting. *ACS Appl. Mater. Interfaces* **2013**, *5*, 5269−5275.

(38) Takai, A.; Kamat, P. V. Capture, Store, and Discharge. Shuttling Photogenerated Electrons across TiO2−Silver Interface. *ACS Nano* **2011**, *5*, 7369−7376.

(39) Zhou, L.; Boyd, C. E. Comparison of Nessler, Phenate, Salicylate and Ion Selective Electrode Procedures for Determination of Total Ammonia Nitrogen in Aquaculture. *Aquaculture* **2016**, *450*, 187−193.

(40) Bernardes, J. C.; Müller, D.; Pinheiro, G. K.; Rambo, C. R. Enhancing the Optical Transparency of TiO2 Aerogels with High Surface Area through Water-Based Synthesis. *Opt. Mater.* **2020**, *109*, 110359.

(41) Alwin, S.; Ramasubbu, V.; Shajan, X. TiO2 Aerogel−metal Organic Framework Nanocomposite: A New Class of Photoanode

1064 Material for Dye-Sensitized Solar Cell Applications. *Bull. Mater. Sci.*
1065 **2018**, *41*, 27.

1066 (42) Quintero, Y.; Mosquera, E.; Diosa, J.; García, A. Ultrasonic-
1067 Assisted Sol−gel Synthesis of TiO2 Nanostructures: Influence of
1068 Synthesis Parameters on Morphology, Crystallinity, and Photo-
1069 catalytic Performance. *J. Sol-Gel Sci. Technol.* **2020**, *94*, 477−485.

1070 (43) Moussaoui, R.; Elghniji, K.; ben Mosbah, M.; Elaloui, E.;
1071 Moussaoui, Y. Sol−gel Synthesis of Highly TiO2 Aerogel Photo-
1072 catalyst via High Temperature Supercritical Drying. *J. Saudi Chem.*
1073 *Soc.* **2017**, *21*, 751−760.

1074 (44) Kandiel, T. A.; Dillert, R.; Robben, L.; Bahnemann, D. W.
1075 Photonic Efficiency and Mechanism of Photocatalytic Molecular
1076 Hydrogen Production over Platinized Titanium Dioxide from
1077 Aqueous Methanol Solutions. *Catal. Today* **2011**, *161*, 196−201.

1078 (45) Ohsaka, T.; Yamaoka, S.; Shimomura, O. Effect of Hydrostatic
1079 Pressure on the Raman Spectrum of Anatase (TiO2). *Solid State*
1080 *Commun.* **1979**, *30*, 345−347.

1081 (46) Balachandran, U.; Eror, N. G. Raman Spectra of Titanium
1082 Dioxide. *J. Solid State Chem.* **1982**, *42*, 276−282.

1083 (47) Kelly, S.; Pollak, F. H.; Tomkiewicz, M. Raman Spectroscopy as
1084 a Morphological Probe for TiO2 Aerogels. *J. Phys. Chem. B* **1997**, *101*,
1085 2730−2734.

1086 (48) Swamy, V.; Kuznetsov, A.; Dubrovinsky, L. S.; Caruso, R. A.;
1087 Shchukin, D. G.; Muddle, B. C. Finite-Size and Pressure Effects on the
1088 Raman Spectrum of Nanocrystalline Anatase Ti O2. *Phys. Rev. B:*
1089 *Condens. Matter Mater. Phys* **2005**, *71*, 184302.

1090 (49) Niilisk, A.; Moppel, M.; Pärs, M.; Sildos, I.; Jantson, T.;
1091 Avarmaa, T.; Jaaniso, R.; Aarik, J. Structural Study of TiO2 Thin
1092 Films by Micro-Raman Spectroscopy. *Cent. Eur. J. Phys.* **2006**, *4*,
1093 105−116.

1094 (50) Thommes, M.; Kaneko, K.; Neimark, A. V.; Olivier, J. P.;
1095 Rodriguez-Reinoso, F.; Rouquerol, J.; Sing, K. S. W. *IUPAC Technical*
1096 *Report Physisorption of Gases, with Special Reference to the Evaluation of*
1097 *Surface Area and Pore Size Distribution (IUPAC Technical Report)*;
1098 2015.

1099 (51) Schlumberger, C.; Thommes, M. Characterization of Hierarchi-
1100 cally Ordered Porous Materials by Physisorption and Mercury
1101 Porosimetry—A Tutorial Review. *Adv. Mater. Interfaces* **2021**, *8*,
1102 2002181.

1103 (52) Bardestani, R.; Patience, G. S.; Kaliaguine, S. Experimental
1104 Methods in Chemical Engineering: Specific Surface Area and Pore
1105 Size Distribution measurements—BET, BJH, and DFT. *Can. J. Chem.*
1106 *Eng.* **2019**, *97*, 2781−2791.

1107 (53) Voepel, P.; Weiss, M.; Smarsly, B. M.; Marschall, R.
1108 Photocatalytic Activity of Multiphase TiO2(B)/anatase Nanoparticle
1109 Heterojunctions Prepared from Ionic Liquids. *J. Photochem. Photobiol.,*
1110 *A* **2018**, *366*, 34−40.

1111 (54) Lin, C. C.; Wei, T. Y.; Lee, K. T.; Lu, S. Y. Titania and Pt/
1112 titania Aerogels as Superior Mesoporous Structures for Photocatalytic
1113 Water Splitting. *J. Mater. Chem.* **2011**, *21*, 12668−12674.

1114 (55) Dette, C.; Pérez-Osorio, M. A.; Kley, C. S.; Punke, P.; Patrick,
1115 C. E.; Jacobson, P.; Giustino, F.; Jung, S. J.; Kern, K. TiO2 Anatase
1116 with a Bandgap in the Visible Region. *Nano Lett.* **2014**, *14*, 6533−
1117 6538.

1118 (56) Zywitzki, D.; Jing, H.; Tüysüz, H.; Chan, C. K. High Surface
1119 Area, Amorphous Titania with Reactive Ti3+ through a Photo-
1120 Assisted Synthesis Method for Photocatalytic H2 Generation. *J.*
1121 *Mater. Chem. A* **2017**, *5*, 10957−10967.

1122 (57) Kong, M.; Li, Y.; Chen, X.; Tian, T.; Fang, P.; Zheng, F.; Zhao,
1123 X. Tuning the Relative Concentration Ratio of Bulk Defects to
1124 Surface Defects in TiO2 Nanocrystals Leads to High Photocatalytic
1125 Efficiency. *J. Am. Chem. Soc.* **2011**, *133*, 16414−16417.

1126 (58) Kiwi, J.; Graetzel, M. Optimization of Conditions for
1127 Photochemical Water Cleavage. Aqueous Pt/TiO2 (Anatase)
1128 Dispersions under Ultraviolet Light. *J. Phys. Chem.* **1984**, *88*, 1302−
1129 1307.

1130 (59) Furube, A.; Asahi, T.; Masuhara, H.; Yamashita, H.; Anpo, M.
1131 Direct Observation of a Picosecond Charge Separation Process in
1132 Photoexcited Platinum-Loaded TiO2 Particles by Femtosecond

1133 Diffuse Reflectance Spectroscopy. *Chem. Phys. Lett.* **2001**, *336*,
1134 424−430.

1135 (60) Ikeda, S.; Sugiyama, N.; Murakami, S.; Kominami, H.; Kera, Y.;
1136 Noguchi, H.; Uosaki, K.; Torimoto, T.; Ohtani, B. Quantitative
1137 Analysis of Defective Sites in titanium(IV) Oxide Photocatalyst
1138 Powders. *Phys. Chem. Chem. Phys.* **2003**, *5*, 778−783.

1139 (61) Yan, J.; Wu, G.; Guan, N.; Li, L.; Li, Z.; Cao, X. Understanding
1140 the Effect of Surface/bulk Defects on the Photocatalytic Activity of
1141 TiO2: Anatase versus Rutile. *Phys. Chem. Chem. Phys.* **2013**, *15*,
1142 10978.

1143 (62) Yang, J.; Wang, D.; Han, H.; Li, C. Roles of Cocatalysts in
1144 Photocatalysis and Photoelectrocatalysis. *Acc. Chem. Res.* **2013**, *46*,
1145 1900−1909.

1146 (63) Trasatti, S. Work Function, Electronegativity, and Electro-
1147 chemical Behaviour of Metals. *J. Electroanal. Chem. Interfacial*
1148 *Electrochem.* **1972**, *39*, 163−184.

1149 (64) Ziegenbalg, D.; Zander, J.; Marschall, R. Photocatalytic
1150 Nitrogen Reduction: Challenging Materials with Reaction Engineer-
1151 ing. *ChemPhotoChem* **2021**, *5*, 792−807.

1152 (65) Cheng, M.; Xiao, C.; Xie, Y. Photocatalytic Nitrogen Fixation:
1153 The Role of Defects in Photocatalysts. *J. Mater. Chem. A* **2019**, *7*,
1154 19616−19633.

1155 (66) Li, C.; Wang, T.; Zhao, Z.-J.; Yang, W.; Li, J.-F.; Li, A.; Yang,
1156 Z.; Ozin, G. A.; Gong, J. Promoted Fixation of Molecular Nitrogen
1157 with Surface Oxygen Vacancies on Plasmon-Enhanced TiO₂ Photo-
1158 electrodes. *Angew. Chem.* **2018**, *130*, 5376−5380.